Inorganic Chemistry
Article
pubs.acs.org/IC

$Pb_7Bi_4Se_{13}$: A Lillianite Homologue with Promising Thermoelectric Properties

Alan Olvera,[†,‡] Guangsha Shi,[†,‡] Honore Djieutedjeu,[†,‡] Alexander Page,[§] Ctirad Uher,[§] Emmanouil Kioupakis,*,[†] and Pierre F. P. Poudeu*,[†]

[†]Department of Materials Science and Engineering and [§]Department of Physics, University of Michigan, Ann Arbor, Michigan 48109, United States

Supporting Information

ABSTRACT: $Pb_7Bi_4Se_{13}$ crystallizes in the monoclinic space group $C2/m$ (No. 12) with a = 13.991(3) Å, b = 4.262(2) Å, c = 23.432(5) Å, and β = 98.3(3)° at 300 K. In its three-dimensional structure, two NaCl-type layers A and B with respective thicknesses N_1 = 5 and N_2 = 4 [N = number of edge-sharing (Pb/Bi)Se_6 octahedra along the central diagonal] are arranged along the c axis in such a way that the bridging monocapped trigonal prisms, $PbSe_7$, are located on a pseudomirror plane parallel to (001). This complex atomic-scale structure results in a remarkably low thermal conductivity (~0.33 W m^{-1} K^{-1} at 300 K). Electronic structure calculations and diffuse-reflectance measurements indicate that $Pb_7Bi_4Se_{13}$ is a narrow-gap semiconductor with an indirect band gap of 0.23 eV. Multiple peaks and valleys were observed near the band edges, suggesting that $Pb_7Bi_4Se_{13}$ is a promising compound for both n- and p-type doping. Electronic-transport data on the as-grown material reveal an n-type degenerate semiconducting behavior with a large thermopower (~−160 μV K^{-1} at 300 K) and a relatively low electrical resistivity. The inherently low thermal conductivity of $Pb_7Bi_4Se_{13}$ and its tunable electronic properties point to a high thermoelectric figure of merit for properly optimized samples.

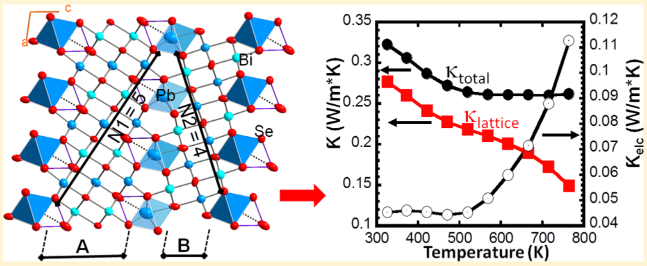

INTRODUCTION

Binary and multinary heavy main-group metal chalcogenides have emerged over the past decades as promising systems for the search of high-performance materials for various renewable energy applications including thermoelectrics[1−4] and photovoltaics.[5,6] The strong interest in these families of compounds is driven by their ability to form a large variety of complex homologous structures with compositional flexibility. These structural features enable a relatively facile manipulation of the physical properties of main-group metal chalcogenides through controlled alteration of the crystal structure and/or chemical composition and also offer the possibility of integrating magnetic and semiconducting functionalities within the same crystal lattice.[7−9]

Known homologous series in the main-group metal chalcogenide systems include both synthetic and naturally occurring series of structures. Structurally characterized synthetic homologous series encompass families of quaternary compounds such as (1) $A_m[M_{1+l}Se_{2+l}]_{2m}[M_{2l+n}Se_{2+3l+n}]$ (A = K, Rb, Cs; M = Sn, Pb)[10,11] in which various members are structurally characterized by three independent integers l, m, and n and (2) $[BiQX]_2[Ag_xBi_{1-x}Q_{2-2x}X_{2x-1}]_{N+1}$ (Q = S, Se; X = Cl, Br; ${}^1/_2 \leq x \leq 1$) where known members are structurally distinguished by the thickness of the NaCl-type structural module, which is defined by the number N ($N \geq 0$) of edge-sharing octahedra running across its central diagonal.[12,13] Examples of naturally occurring homologous series are sulfosalts such as the pavonite homologous series with the general formula $M_{N+1}Bi_2S_{N+5}$ (M = Ag/Bi or Cu/Bi; $N \geq 2$)[14] and the lillianite series.[15] Most known members of the lillianite homologous series are minerals with the general chemical formula $Pb_{N-1-2x}Bi_{2+x}Ag_xS_{N+2}$.[15] In the structure of lillianite homologues, two NaCl-type layered modules denoted as A and B with thicknesses N_1 and N_2 (where N_1 and N_2 are the number of edge-sharing octahedra that run across the central diagonal of adjacent modules) are "twinned" on $[PbS_{6+2}]$ bicapped trigonal prisms.[15] Lillianite homologues are distinguished by the thicknesses N_1 and N_2 of the NaCl-type modules and therefore are denoted by ${}^{N_1,N_2}L$.

Despite the well-established relationship between the structure and composition of lillianite homologues, the number of structurally characterized members is quite small. For instance, known lillianite homologues in the Pb−Bi−Ag−S system are ${}^{4,4}L$, ${}^{4,7}L$, ${}^{4,8}L$, ${}^{7,7}L$, ${}^{5,9}L$, ${}^{8,8}L$, and ${}^{11,11}L$ with the general formula $Pb_{N-1-2x}Bi_{2+x}Ag_xS_{N+2}$ [$N = (N_1 + N_2)/2$].[15,16] Ag-free ternary lillianite homologues (x = 0) with the general formula $Pb_{N-1}Bi_2S_{N+2}$ are also stable. Some examples of naturally occurring compositions that have been fully characterized to date include lillianite, $Pb_3Bi_2S_6$ (${}^{4,4}L$),[17]

Special Issue: To Honor the Memory of Prof. John D. Corbett

Received: June 9, 2014
Published: August 4, 2014

dx.doi.org/10.1021/ic501327u | Inorg. Chem. 2015, 54, 746−755

heyrovskyite, $Pb_6Bi_2S_9$ ($^{7,7}L$)[18] and galenobismutite, $PbBi_2S_4$ ($^{2,2}L$).[19] However, several homologous structures that could be predicted from the general formula $Pb_{N-1}Bi_2S_{N+2}$ are still missing. Furthermore, it appears that only a small number of selenium analogues of the lillianite homologous series $Pb_{N-1}Bi_2Se_{N+2}$ have been reported so far. Known structurally characterized members include α-$Pb_6Bi_2Se_9$,[20] $Pb_2Bi_2Se_5$,[21] $PbBi_2Se_4$,[22] and $Pb_3Bi_4Se_9$.[23] Beyond members of the $Pb_{N-1}Bi_2Se_{N+2}$ homologous series, various stable ternary $(PbSe)_m(Bi_2Se_3)_n$ phases with structures composed of alternating layers of Bi_2Se_3- and PbSe-type fragments in various ratios, such as $Pb_5Bi_6Se_{14}$,[20,24,25] $Pb_5Bi_{12}Se_{23}$,[20,25] and $Pb_5Bi_{18}Se_{32}$,[25] have also been reported in the pseudobinary PbSe−Bi_2Se_3 phase diagram.[25]

The lack of interest in synthesizing and characterizing $Pb_{N-1}Bi_2Se_{N+2}$ phases is presumably due to the rather large band gap of $(PbS)_m(Bi_2S_3)_n$ phases (PbS, 0.4 eV; Bi_2S_3, 1.6 eV; $PbBi_2S_4$, 1.5 eV).[26−28] However, substituting S by Se can drastically reduce the band gap of $Pb_{N-1}Bi_2Se_{N+2}$ phases, leading to a family of semiconducting compounds. For example, narrow band gap ($E_g \sim 0.34$ eV) and promising room temperature values of thermopower ($-133.5\ \mu V\ K^{-1}$) and electrical conductivity ($502.4\ S\ cm^{-1}$) were reported for α-$Pb_6Bi_2Se_9$.[20] By rewriting the general formula in terms of the pseudobinary system $(PbSe)_{N-1}(Bi_2Se_3)$, one can anticipate the ability to tune both the crystal structures and electronic properties of various $Pb_{N-1}Bi_2Se_{N+2}$ phases by adjusting the PbSe/Bi_2Se_3 ratio in the starting mixture. It has been demonstrated that PbSe[4,29] and Bi_2Se_3[30] possess promising thermoelectric properties when properly doped. By fusing the structures of these two compounds into a homologous series of crystal structures, one can anticipate interesting electronic behavior for the resulting $Pb_{N-1}Bi_2Se_{N+2}$ phases. In addition, the heavy weight nature of the constituent elements suggests a low lattice thermal conductivity for the $Pb_{N-1}Bi_2Se_{N+2}$ phases due to the large average molecular weight (AMW) of the compounds [AMW = $(286.16N + 368.68)/(2N + 3)$], which increases with rising N values. Therefore, a promising thermoelectric performance can be anticipated for various $Pb_{N-1}Bi_2Se_{N+2}$ phases. Here, we report the synthesis, crystal structure, electronic band structure, and electronic- and thermal-transport properties of $Pb_7Bi_4Se_{13} \equiv 2(Pb_{3.5}Bi_2Se_{6.5})$, a new member of the $Pb_{N-1}Bi_2Se_{N+2}$ lillianite homologous series featuring the $^{4,5}L$ structure. Differential scanning calorimetry (DSC) revealed that the compound melts congruently at 562 °C and decomposes above 700 °C. We show using charge-transport measurements and electronic structure calculations that the as-grown $Pb_7Bi_4Se_{13}$ is a narrow-band-gap n-type semiconductor combining inherently ultralow thermal conductivity and promising electronic properties.

■ EXPERIMENTAL SECTION

Synthesis. Single crystals of $Pb_7Bi_4Se_{13}$ were obtained from a solid-state reaction involving high-purity elemental powders, lead metal powder (CERAC, 99.8%), bismuth metal pieces (Aldrich, 99.999%), and selenium powder (CERAC, 99.999%) in the desired ratio (total mass = 5 g). A mixture of the starting reagents was loaded into a fused silica tube (⌀ = 7 mm; length = 20 cm) under an argon atmosphere, and the tube was flame-sealed under a residual pressure of $\sim 10^{-3}$ Torr. The sealed tube was loaded into a tube furnace, heated slowly to 573 K over 12 h, and held at that temperature for 48 h to allow complete melting of bismuth and selenium and reaction with the remaining lead powder. The temperature was then ramped up to 773 K and held constant for 72 h in order to improve the crystallinity of the product and also to promote crystal growth. Several needle-shaped black single crystals suitable for X-ray structure determination were selected from the resulting polycrystalline sample. For charge-transport measurements, high-purity polycrystalline powder of $Pb_7Bi_4Se_{13}$ was synthesized by mechanical alloying of elemental powder in the desired stoichiometry (total mass = 5 g) using high-energy shaker ball milling. The polycrystalline powder obtained after 6 h of mechanical alloying was subsequently annealed at 773 K for 14 days and hot pressed into a high-density (97%) pellet for property measurements.

Characterization. *Powder X-ray Diffraction.* The phase purity of $Pb_7Bi_4Se_{13}$ polycrystalline samples was assessed by comparing the X-ray diffraction pattern on finely ground powder (recorded using monochromated Cu Kα radiation on a rotating-anode Rigaku powder diffractometer operating under 40 kV and 40 mA) with the theoretical pattern simulated using single-crystal structure data.

DSC. To further confirm the phase purity of the synthesized $Pb_7Bi_4Se_{13}$ compound and also to determine its melting temperature, DSC was performed on a finely ground powder. DSC data were recorded on a F401 DSC apparatus (NETZSCH) using approximately 25 mg of the synthesized material and an equivalent mass of alumina (Al_2O_3) as the reference, following procedures described elsewhere.[8] The sample and reference were simultaneously heated to 1073 K at a rate of 20 K min^{-1}, isothermed for 2 min, and then cooled to 473 K at a rate of 20 K min^{-1}.

Diffuse Reflectance. The optical band gap of $Pb_7Bi_4Se_{13}$ was probed at room temperature in the 4000−400 cm^{-1} wavenumber region using a PerkinElmer Frontier Fourier transform infrared/near-IR spectrometer. The reflectance data were converted into absorption data using the Kubelka−Munk function $\alpha/S = (1 - R)^2/2R$[31] (where R is the reflectance at a given wavelength, α is the absorption coefficient, and S is the scattering coefficient), and the optical band gap was estimated from an absorption (α/S) versus energy plot.[31,32]

Crystal Structure Determination. A single crystal of $Pb_7Bi_4Se_{13}$ (0.01 × 0.03 × 0.08 mm) was mounted on the tip of a glass fiber using epoxy glue, and the intensity data were recorded at 100 and 300 K on a STOE IPDS-2T diffractometer using a graphite-monochromated Mo Kα radiation (λ = 0.71073 Å). The intensity data at both temperatures were best indexed in the monoclinic crystal system with unit cell parameters: a = 13.933(2) Å, b = 4.246 (1) Å, c = 23.296(2) Å, and β = 98.0(1)° at 100 K and a = 13.991(3) Å, b = 4.262(2) Å, c = 23.432(5) Å, and β = 98.3(3)° at 300 K, with Z = 2. The structure solution at 300 K was obtained by direct methods in the $C2/m$ (No. 12) space group and refined by full-matrix least-squares techniques using the *SHELTXL* package.[33] Six crystallographically independent metal positions (Bi1−Bi6) and seven Se-atom positions (Se1−Se7) were found in the unit cell. The refinement of this model yielded $R_1 \sim$ 8% with reasonable thermal parameters for all atoms. However, the resulting composition of the crystal ($Bi_{11}Se_{13}$) exhibits a large excess of positive charges, suggesting that some of the Bi positions are occupied by Pb atoms. Because the Bi and Pb positions are not distinguishable using X-ray diffraction data, bond valence sum (BVS)[34] calculations were performed assuming full occupation of each metal site by either Bi or Pb. The results of the BVS calculations (Table 1) enabled the final distribution of Pb and Bi atoms within the various metal positions and also confirmed their oxidation states. Bi1, Bi(2), Pb(2), and Pb(3) atoms were located at the octahedrally coordinated general positions (4i), and the Pb(1) atom was located at the 6-fold special position 2b

Table 1. BVS Calculations for $Pb_7Bi_4Se_{13}$ at 300 K

atomic position	BVS	atom type	oxidation state
Bi(1)	3.03	Bi	3+
Bi(2)	3.17	Bi	3+
Pb(1)	2.11	Pb	2+
Pb(2)	2.20	Pb	2+
Pb(3)	2.30	Pb	2+
Pb(4)	1.95	Pb	2+

($^1/_2$, 0, 0). These octahedrally coordinated metal atoms build two NaCl-type layers denoted as A and B with different thicknesses. The Pb(4) atom occupied the 7-fold-coordinated general position (4i) linking adjacent NaCl-type layers. The refinement of the final model while including a secondary extinction correction and anisotropic displacement parameters for all atoms resulted in a final $R_1 \sim 2.9\%$. The final charge-balanced composition of the crystal obtained from the refinement was $(Pb^{2+})_7(Bi^{3+})_4(Se^{2-})_{13}$. A parallel refinement of the structure of $Pb_7Bi_4Se_{13}$ at 100 K revealed no major structural change, and the distributions of Pb and Bi atoms at the metal positions within the structure were similar to those obtained at 300 K. A summary of the crystallographic data is given in Table 2. The atomic coordinates and isotropic displacement parameters of all atoms are given in Table 3. Selected interatomic distances are gathered in Table 4. The software *Diamond*[35] was utilized to create the graphic representation of the crystal structure with ellipsoid representations (98% probability level) for all atoms. Detailed crystallographic data can be obtained from Fachinformationszentrum Karlsruhe, 76344 Eggenstein-Leopoldshafen, Germany (fax +49-7247-808-666; e-mail crysdata@fiz.karlsruhe.de), on quoting the depository number CSD-427410 for $Pb_7Bi_4Se_{13}$ at 100 K and CSD-427411 for $Pb_7Bi_4Se_{13}$ at 300 K.

Table 2. Selected Crystallographic Data for $Pb_7Bi_4Se_{13}$ at 100 and 300 K

	100 K	300 K
cryst syst; space group	monoclinic; $C2/m$ (No. 12)	
fw (g mol^{-1})	3312.73	
density calcd (g cm^{-3})	8.06	7.96
lattice parameters (Å)		
a	13.933(2)	13.991(3)
b	4.246(1)	4.262(2)
c	23.296(2)	23.432(5)
β (deg)	98.0(1)	98.3(3)
V (Å^3); Z	1364.74 (4); 2	1382.54(4); 2
radiation (Å)	λ(Mo Kα) = 0.71073	
μ (cm^{-1})	860	849
2θ range	$6° \leq 2\theta \leq 58°$	$5° \leq 2\theta \leq 63°$
index range	$-18 \leq h \leq 17$	$-18 \leq h \leq 18$
	$-5 \leq k \leq 5$	$-6 \leq k \leq 6$
	$-31 \leq l \leq 31$	$-30 \leq l \leq 30$
transmission factors	0.06−0.42	0.03−0.40
diff electron density [e Å^{-3}]	+4.44 to −2.73	+4.43 to −2.85
R1 [$F_o > 4\sigma(F_o)$][a]	0.029	0.029
wR2 (all)[b]	0.074	0.073
GOF	1.126	1.176

[a] $R1 = \sum||F_o| - |F_c||/\sum|F_o|$. [b] $wR2 = [\sum w(F_o^2 - F_c^2)^2/\sum w(F_o^2)^2]^{1/2}$.

First-Principles Calculations. We studied the electronic properties of $Pb_7Bi_4Se_{13}$ with calculations based on density functional theory (DFT) and many-body perturbation theory. DFT calculations were performed using the local-density approximation for the exchange-correlation potential to obtain the ground-state charge density and electronic wave functions.[36] We employed the plane-wave pseudopotential method[37] with a plane-wave cutoff of 60 Ry and norm-conserving pseudopotentials,[38] as implemented in the *Quantum-ESPRESSO* code.[39] The 5d states of Pb are needed to calculate an accurate band gap for PbSe (0.144 eV) and are included in the valence. The 5d electrons of Bi are frozen in the pseudopotential core because this has been shown to accurately reproduce the band gaps of Bi_2Se_3 and Bi_2Te_3.[40,41] For the calculations, we used the experimental values for the lattice vectors and atomic positions of $Pb_7Bi_4Se_{13}$ (from Tables 2 and 3). We sampled the Brillouin zone with a 6 × 4 × 1 Monkhorst−Pack grid.[42] The band structure was calculated using the one-shot GW method[43] and the *BerkeleyGW* code.[44] The static dielectric function was calculated with a 15 Ry plane-wave cutoff and extended to finite frequency using the generalized plasmon-pole model of Hybertsen and Louie.[45] The Coulomb-hole self-energy term was calculated using a sum over unoccupied bands of up to 4.3 Ry above the valence band maximum using the static-remainder approach.[46] Corrections due to spin−orbit coupling interaction[43] were calculated in a non-self-consistent way using plane waves up to a cutoff energy of 40 Ry. We used the maximally localized Wannier function formalism to interpolate the quasiparticle energies to arbitrary points in the first Brillouin zone.[39]

Table 3. Wyckoff Positions (WP), Atomic Coordinates, and Equivalent Isotropic Displacement Parameters ($U_{eq}/10^{-4}$ Å^2) for All Atoms in the Asymmetric Unit of $Pb_7Bi_4Se_{13}$ at 100/*300* K

atom	WP	x	y	z	U_{eq}
Bi(1)	4i	0.2481(2)	0	0.0859(2)	87(3)
		0.2496(2)	0	*0.0857(2)*	*225(5)*
Bi(2)	4i	0.5608(2)	$^1/_2$	0.3774(2)	119(3)
		0.5597(2)	$^1/_2$	*0.3775(2)*	*263(6)*
Pb(1)	2b	$^1/_2$	0	0	110(4)
		$^1/_2$	0	0	*268(7)*
Pb(2)	4i	0.8531(2)	$^1/_2$	0.4565(2)	94(3)
		0.8524(2)	$^1/_2$	*0.4563(2)*	*221(5)*
Pb(3)	4i	0.4908(2)	$^1/_2$	0.1625(2)	102(3)
		0.4934(2)	$^1/_2$	*0.1627(2)*	*259(6)*
Pb(4)	4i	0.7678(2)	0	0.2800(2)	220(4)
		0.7672(2)	0	*0.2778(2)*	*475(8)*
Se(1)	4i	0.3710(3)	$^1/_2$	0.0406(2)	72(5)
		0.3712(4)	$^1/_2$	*0.0406(2)*	*174(9)*
Se(2)	4i	0.6232(3)	0	0.1206(2)	137(7)
		0.6250(5)	0	*0.1214(3)*	*297(9)*
Se(3)	4i	0.7134(3)	0	0.4133(2)	118(7)
		0.7114(5)	0	*0.4135(3)*	*244(9)*
Se(4)	4i	0.3617(2)	0	0.1948(2)	97(6)
		0.3648(4)	0	*0.1947(2)*	*221(9)*
Se(5)	4i	0.9191(3)	$^1/_2$	0.3476(2)	94(6)
		0.9178(4)	$^1/_2$	*0.3476(2)*	*209(9)*
Se(6)	2c	0	0	$^1/_2$	71(6)
		0	0	$^1/_2$	*216(9)*
Se(7)	4i	0.6227(3)	$^1/_2$	0.2690(2)	114(6)
		0.6220(5)	$^1/_2$	*0.2696(2)*	*241(9)*

U_{eq} is defined as one-third of the trace of the orthogonalized U_{ij} tensor.

Transport Property Measurement. The Seebeck coefficient and electrical resistivity were measured simultaneously from room temperature to 775 K under a low-pressure helium atmosphere using a commercial ZEM-3 system from ULVAC-RIKO. The instrument precision on the electrical resistivity and Seebeck coefficient data is ±4%. The thermal conductivity was calculated from the thermal diffusivity data measured by the laser flash method (LINSEIS; LFA 1000) from 303 to 775 K under dynamic vacuum (~10^{-3} Torr). The instrument precision on the thermal diffusivity data is ±6%. The pyroceram reference material was measured alongside each sample. The specific heat capacity (C_p) used for thermal conductivity ($\kappa = DC_pd$, where d is the geometrical density of the pellet) calculations were extracted from the laser flash data. The Hall coefficient data were measured in the temperature range from 100 to 300 K under the magnetic field of 1 T using the Quantum Design Physical Properties Measurement System. The carrier density (n) and mobility (μ) were derived using the Hall coefficient and electrical conductivity (σ) data.

■ RESULTS AND DISCUSSION

Synthesis and Characterization. Polycrystalline powders of $Pb_7Bi_4Se_{13}$ were obtained from direct combination of the elements via mechanical alloying using a high-energy shaker

Table 4. Selected Interatomic Distances (Å) in $Pb_7Bi_4Se_{13}$ at 100/300 K[a]

bond type	100 K	300 K
Bi(1)–Se(4)	2.796(3)	2.817(6)
Bi(1)–Se($2^{i,ii}$)	2.928(3)	2.950(5)
Bi(1)–Se($1,1^{iii}$)	3.009(3)	3.012(4)
Bi(1)–Se(1^{iv})	3.176(3)	3.189(6)
Bi(2)–Se(7)	2.779(4)	2.789(6)
Bi(2)–Se($5^{i,ii}$)	2.917(3)	2.927(4)
Bi(2)–Se($3,3^{v}$)	3.038(3)	3.040(5)
Bi(2)–Se(6^{vi})	3.090(2)	3.104(2)
Pb(1)–Se($1,1^{iii,vii,viii}$)	3.017(2)	3.031(4)
Pb(1)–Se($2,2^{viii}$)	3.082(4)	3.117(7)
Pb(2)–Se(5)	2.816(4)	2.827(6)
Pb(2)–Se($3,3^{v}$)	2.961(3)	2.977(5)
Pb(2)–Se($6^{ix,x}$)	3.025(2)	3.041(2)
Pb(2)–Se(3^{xi})	3.292(4)	3.301(7)
Pb(3)–Se(7)	2.876(3)	2.865(7)
Pb(3)–Se($4,4^{v}$)	2.946(2)	2.954(4)
Pb(3)–Se($2,2^{v}$)	3.059(3)	3.063(5)
Pb(3)–Se(1)	3.090(3)	3.115(6)
Pb(4)–Se($7,7^{iii}$)	2.918(3)	2.932(5)
Pb(4)–Se($5,5^{iii}$)	3.242(3)	3.265(5)
Pb(4)–Se(3)	3.295(4)	3.311(5)
Pb(4)–Se($4^{vi,xii}$)	3.299(3)	3.311(5)
Pb(4)···Se(2)	*3.973(4)*	*3.908(8)*

[a] Operators for generating equivalent atoms: (i) $-^1/_2 + x, -^1/_2 + y, z$; (ii) $-^1/_2 + x, ^1/_2 + y, z$; (iii) $x, -1 + y, z$; (iv) $^1/_2 - x, ^1/_2 - y, -z$; (v) $x, 1 + y, z$; (vi) $^1/_2 + x, ^1/_2 + y, z$; (vii) $1 - x, 1 - y, -z$; (viii) $1 - x, -y, -z$; (ix) $1 + x, 1 + y, z$; (x) $1 + x, y, z$; (xi) $^3/_2 - x, ^1/_2 - y, 1 - z$; (xii) $^1/_2 + x, -^1/_2 + y, z$.

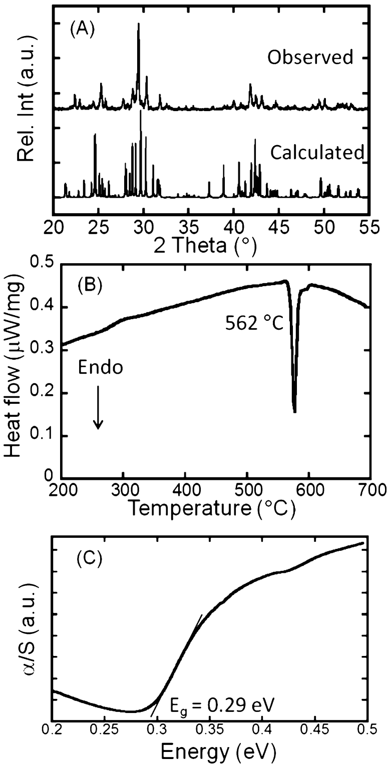

Figure 1. (A) Comparison of the experimental powder X-ray diffraction pattern of $Pb_7Bi_4Se_{13}$ with the theoretical pattern calculated using crystal structure data. (B) DSC of the synthesized material showing a single endothermic peak of congruent melting upon heating. (C) Diffuse-reflectance optical absorption spectrum of $Pb_7Bi_4Se_{13}$ showing the optical band gap of 0.29 eV.

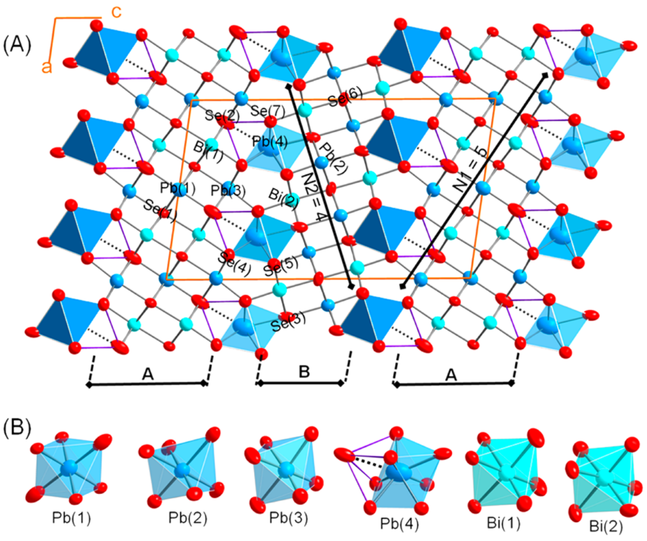

Figure 2. (A) Crystal structure of $Pb_7Bi_4Se_{13}$ projected along the *b* axis highlighting the two NaCl-type layers A and B alternating along the *c* axis. (B) Coordination environment of the metal atoms in the crystal structure.

mill. The crystallinity of the final product was improved by annealing the ball-milled powder at 500 °C for 14 days. A comparison of the X-ray diffraction pattern of the reaction product with the theoretical pattern calculated using single-crystal structure data (Figure 1A) suggested successful formation of the $Pb_7Bi_4Se_{13}$ phase. However, the mismatch of the peak intensities on the experimental and theoretical patterns suggests a very poor crystallinity of the as-synthesized material despite the long annealing step at 500 °C. The single-phase nature of the synthesized $Pb_7Bi_4Se_{13}$ powders was confirmed by DSC (Figure 1B). The material melts congruently at 562 °C and decomposes at temperatures above 700 °C. A crystallization peak was observed at 558 °C upon cooling the melt from 600 °C to room temperature.

Crystal Structure. $Pb_7Bi_4Se_{13}$ crystallizes in the monoclinic space group *C*2/*m* (No. 12) with $a = 13.991(3)$ Å, $b = 4.262(2)$ Å, $c = 23.432(5)$ Å, and $\beta = 98.3(3)°$ (Table 2) and adopts the $KSn_5Bi_5Se_{13}$ structure type.[47] More generally, the structure of $Pb_7Bi_4Se_{13}$ can be classified as the $^{(4,5)}$L member of the lillianite homologous series.[16] The crystal structure (Figure 2A) can be subdivided into two NaCl-type layers denoted as A and B with different thicknesses. Both NaCl-type layers are built by edge-sharing distorted octahedral polyhedra around Bi and Pb atoms. The layers can be distinguished by the number (N) of metal atoms along its central diagonal. Along this line, it can be observed from Figure 2A that layer A consists of five metal sites ($N_1 = 5$), three Pb atoms and two Bi atoms, alternating along its diagonal, whereas layer B contains only four metal sites ($N_2 = 4$), two Bi and two Pb atoms. Therefore, $Pb_7Bi_4Se_{13}$ represents the first ternary selenium analogue of the $Pb_{N-1}Bi_2Se_{N+2}$ family of lillianite homologous series with $N = (N_1 + N_2)/2 = 4.5$ ($Pb_7Bi_4Se_{13} = 2Pb_{3.5}Bi_4Se_{6.5}$). Adjacent layers (A and B) in the structure of $Pb_7Bi_4Se_{13}$ are arranged along the *c* axis in such a way that the diagonal chains of metal atoms are related by a pseudomirror symmetry parallel to the *ab* plane and encompassing the Pb(4) atoms. In lillianite structures where layers A and B are of the same thickness ($N_1 = N_2$), such as ^{4,4}L (lillianite, $Pb_3Bi_2S_6$)[15] and ^{8,8}L ($Ag_{2.25}Pb_{2.5}Bi_{4.25}S_{10}$),[16] adjacent NaCl-type layers are related by a mirror symmetry [space group *Cmcm* (No. 63)] and the metal atom located on the mirror plane connecting both layers is coordinated by eight anions in a bicapped trigonal-prismatic geometry. However, in lillianite structures with different thicknesses of layers A and B ($N_1 \neq N_2$), for example, vikingite, $Pb_8Ag_5Bi_{13}S_{30}$ (^{4,7}L), treasurite, $Pb_6Ag_7Bi_{15}S_{32}$ (^{4,8}L), and eskimoite, $Pb_{10}Ag_7Bi_{15}S_{36}$, (^{5,9}L),[16] the mirror symmetry between adjacent layers A and B is broken, resulting in a reduction of the crystal symmetry to the monoclinic space group *C*2/*m* (No. 12). As a consequence, the coordination geometry of the metal atom bridging adjacent layers changes from a bicapped trigonal prism (CN = 8) to a monocapped trigonal prism (CN = 7). Therefore, the bridging Pb(4) atom (Figure 2B and Table 3) in the structure of $Pb_7Bi_4Se_{13}$ is surrounded by seven selenium atoms (CN = 7), forming a distorted [2 + 2 + 1 + 2 + 1] monocapped trigonal prism with Pb---Se bond distances ranging from 2.932(5) to 3.311(5) Å (Table 4). The eighth Se atom, that could serve as the second capping atom [Se(2)], lies at 3.908(8) Å, which is too far to be considered as bonding. Upon cooling, the 100 K Pb(4)---Se(2) bond anomalously expands to 3.973(4) Å, presumably because of the difference in the contraction of both layers (A and B). The remaining metal atoms in the crystal structure of $Pb_7Bi_4Se_{13}$ are located in octahedral sites with various degrees of distortion (Figure 2B and Table 4). While the Pb(1) atom located in the middle of layer A [special position: 2b ($^1/_2$, 0, 0)] displays a nearly perfect octahedral geometry [4 + 2] with four equatorial Pb---Se bonds at 3.031(4) Å and two slightly longer axial Pb---Se bonds at 3.117(7) Å, a more distorted [1 + 2 + 2 + 1] octahedral geometry is observed for the Pb(2), Pb(3), Bi(1), and Bi(2) atoms, which are located toward the borders of the layers (Table 4). This severe distortion of the octahedral shape for Pb^{2+} and Bi^{3+} atoms toward the periphery of the layers is generally attributed to the stereoactivity of their lone pairs.[11] The stereoactivity of the lone pair for the periphery atoms is presumably facilitated by the "free" space along the interfaces between adjacent layers A and B arising from the atomic-scale lattice incoherency between them. Such atomic-scale features are expected to play a major role in the scattering of heat-conducting phonons propagating through the material. In addition, the combination of heavy elements such as Pb, Bi, and Se in the same crystal structure can lead to a significant reduction in the thermal conductivity of the resulting compound. Therefore, one can anticipate a rather low thermal conductivity for $Pb_7Bi_4Se_{13}$ given the chemical composition and structural arrangement of various layers A and B in the crystal structure. From the chemical composition and structural viewpoints, the molecular formula of $Pb_7Bi_4Se_{13}$ can be rewritten as $7(PbSe)\cdot 2(Bi_2Se_3)$. This atomic-scale integration of two promising thermoelectric materials can give rise to very interesting electronic-transport properties.

Electronic Structure. The calculated electronic band structure of $Pb_7Bi_4Se_{13}$ is shown in Figure 3. The band gap of $Pb_7Bi_4Se_{13}$ is found to be indirect with a magnitude of 0.23 eV. The bands exhibit numerous avoided crossings because of the low symmetry of the unit cell and the spin−orbit-coupling interaction. The energies of the band extrema and their positions in the Brillouin zone are summarized in Table 5. The positions of the band extrema are reported in crystal coordinates, and energies are referenced to the valence-band maximum (VBM). The position of the VBM is at *k* = (0.494, 0.372, 0.820). In addition, the band structure exhibits local VBMs, VBM1 at (0.227, 0.061, 0.467) and VBM2 at (0.763, 0.063, 0.467), located just 31 meV lower in energy than the global VBM. Because this energy difference is comparable to k_BT at room temperature (25 meV for *T* = 300 K), all six VBMs contribute to electrical conduction in p-type samples at room temperature and above. The conduction-band minimum (CBM) is located at the *Z* point (0.5, 0, 0.5) of the first Brillouin zone (Figure 4).[48] The minimum direct gap is 0.24 eV and also occurs at the *Z* point.

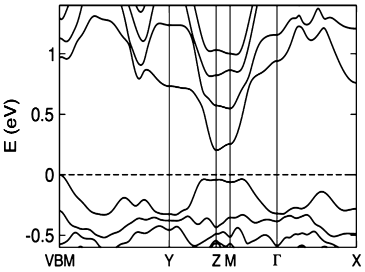

Figure 3. Electronic band structure of $Pb_7Bi_4Se_{13}$. The energy zero corresponds to the VBM and is indicated by the dashed line. The material has an indirect band gap of 0.23 eV, and the minimum direct gap of 0.24 eV occurs at the *Z* point.

Table 5. Calculated values of the locations and energies of the conduction and valence band extrema, angles of the principal axes of the constant-energy ellipsoids, and effective masses along the principal axes of $Pb_7Bi_4Se_{13}$. The locations of the band extrema (k_1, k_2, k_3) are reported in crystal coordinates

extremum	CBM	VBM	VBM1	VBM2
multiplicity	1	2	2	2
(k_1, k_2, k_3)	(0.5, 0, 0.5)	(0.494, 0.372, 0.820)	(0.227, 0.061, 0.467)	(0.763, 0.063, 0.467)
E (eV)	0.23	0	−0.03	−0.03
θ (deg)	2.82	79.3	66	77.4
ϕ (deg)	23.1	93.9	110	106
γ (deg)	46.3	80	107	88.4
m_1^*	0.108	0.792	1.29	1.23
α_1 (eV^{-1})	1.61			
m_2^*	0.0598	0.264	0.929	0.846
α_2 (eV^{-1})	1.36	0.426		
m_3^*	0.612	0.773	0.216	0.217
α_3 (eV^{-1})	2.7		5.81	5.03

The calculated values of the effective mass parameters of $Pb_7Bi_4Se_{13}$ are also listed in Table 5. The band structure near an extremum is given by

$$E(k) = \hbar^2\left(\frac{k_a^{\ 2}}{2m_a} + \frac{k_b^{\ 2}}{2m_b} + \frac{k_c^{\ 2}}{2m_c}\right) \tag{1}$$

and its isosurface has the shape of an ellipsoid. The reciprocal-space Cartesian coordinates along the three principal axes of the constant-energy ellipsoid (k_a, k_b, and k_c) are related to the Cartesian coordinates k_x, k_y, and k_z of the reference system by the transformation matrix[49]

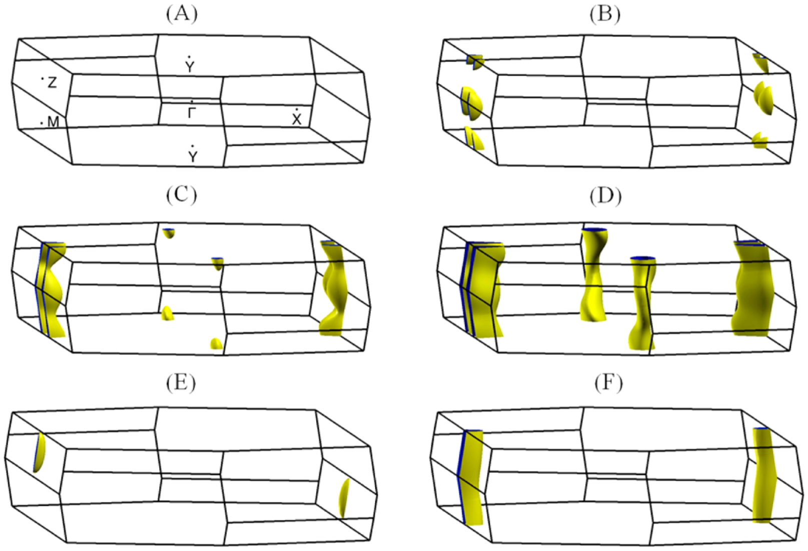

Figure 4. Constant energy surfaces around the valence- and conduction-band extrema of $Pb_7Bi_4Se_{13}$. (A) First Brillouin zone in the TRI_{1b} lattice. (B−D) Constant-energy surfaces of the highest valence band of $Pb_7Bi_4Se_{13}$ with energies of (B) 5, (C) 10, and (D) 25 meV lower than the VBM energy. (E and F) Constant-energy surfaces of the lowest conduction band of $Pb_7Bi_4Se_{13}$ with energies of (E) 20 and (F) 100 meV above the CBM. The shape of the surfaces shows the strong warping of the valence- and conduction-band structures even for energies within a few multiples of k_BT from the band extrema for temperatures of interest for thermoelectric applications (300−800 K).

$$\begin{bmatrix} k_a \\ k_b \\ k_c \end{bmatrix} = \begin{bmatrix} k_x \\ k_y \\ k_z \end{bmatrix} \begin{bmatrix} ll(1-\cos\gamma) & ml(1-\cos\gamma) & nl(1-\cos\gamma) \\ +\cos\gamma & -n\sin\gamma & +m\sin\gamma \\ lm(1-\cos\gamma) & mm(1-\cos\gamma) & nm(1-\cos\gamma) \\ +n\sin\gamma & +\cos\gamma & -l\sin\gamma \\ \mathrm{ln}(1-\cos\gamma) & mn(1-\cos\gamma) & nn(1-\cos\gamma) \\ -m\sin\gamma & +l\sin\gamma & +\cos\gamma \end{bmatrix} \tag{2}$$

where

$$(l, m, n) = (\sin\theta\cos\varphi,\ \sin\theta\sin\varphi,\ \cos\theta) \tag{3}$$

defines the axis of rotation, while θ and ϕ are the polar and azimuthal angles and γ is the angle of rotation. We calculated the effective mass tensors of $Pb_7Bi_4Se_{13}$ by determining the directions of the principal axes of the ellipsoid and the effective mass along each principal axis. The directions of the principal axes are obtained by fitting eqs 1 and 2 to the calculated energy eigenvalues near each band extremum. After we determined the principal axes, a more accurate estimate for the effective mass parameters was obtained by fitting the energy eigenvalues along each principal axis with the hyperbolic equation

$$E(1 + \alpha E) = \frac{\hbar^2 k^2}{m} \tag{4}$$

which accounts for the nonparabolicity of the energy bands at higher energies. The value of $1/\alpha$ indicates the characteristic energy beyond which nonparabolicity is significant.

Our calculations show that the bands of $Pb_7Bi_4Se_{13}$ have a complex structure that cannot be accurately described with a simple effective mass parametrization near the band extrema. Figure 4 shows a set of constant-energy surfaces of the valence and conduction bands of $Pb_7Bi_4Se_{13}$ plotted within the first Brillouin zone. The plots demonstrate the multiple local maxima of the valence band that reside within an energy range of k_BT from the VBM at room temperature. Moreover, the data in Figure 4 show that, even for energies within a few multiples of k_BT from the band extrema for temperatures of interest for thermoelectric applications (300−800 K), the constant-energy surfaces around each local extremum merge into continuous surfaces that span the entire width of the Brillouin zone. Thus, the conduction and valence bands of $Pb_7Bi_4Se_{13}$ cannot be described with an effective mass model for transport calculations in n- and p-type samples at room temperature and above. Instead, the full band structure in the entire Brillouin zone as determined from our first-principles calculations is needed to accurately describe the transport properties of $Pb_7Bi_4Se_{13}$, such as the mobility and Seebeck coefficient.

Charge-Transport Properties. To probe the electronic and thermal behavior of $Pb_7Bi_4Se_{13}$, measurements of the Hall effect and resistivity data from 100 to 300 K and the electrical conductivity, thermopower, and thermal conductivity from 300 to 775 K were performed using a hot-pressed pellet of the synthesized material. Figure 5 shows the temperature dependence of the Hall coefficient (R_H), carrier concentration (n), and carrier mobility (μ). A constant negative value of $R_H \sim -0.65$ $cm^3\ C^{-1}$ is observed in the whole temperature range, indicating that the synthesized $Pb_7Bi_4Se_{13}$ phase is heavily doped with electrons as the majority charge carriers (Figure 5A). Accordingly, a constant carrier density, $n \sim 10^{19}$ cm^{-3} (Figure 5B), was calculated from the R_H data ($n = -1/eR_H$, where e is the electron charge). The carrier mobility ($\mu = \sigma/ne$) extracted using the carrier density and resistivity data decreases with increasing temperature from 120 $cm^2\ V^{-1}\ s^{-1}$ at 100 K to 40 $cm^2\ V^{-1}\ s^{-1}$ at 300 K (Figure 5C). The curve with which the mobility drops with rising temperature can be fitted to the power law $T^{-1.05}$, suggesting that carrier transport in $Pb_7Bi_4Se_{13}$ is affected by acoustic phonon scattering.[50]

Figure 6A shows the temperature dependence of the electrical resistivity and thermopower of $Pb_7Bi_4Se_{13}$. The compound shows negative values of the thermopower in the whole temperature range, indicating that electrons remain the majority charge carriers at temperatures above 300 K. The thermopower at 300 K is −160 $\mu V\ K^{-1}$ and increases rapidly with rising temperature, reaching a maximum of −243 $\mu V\ K^{-1}$ at 600 K, and decreases thereafter with further an increase in

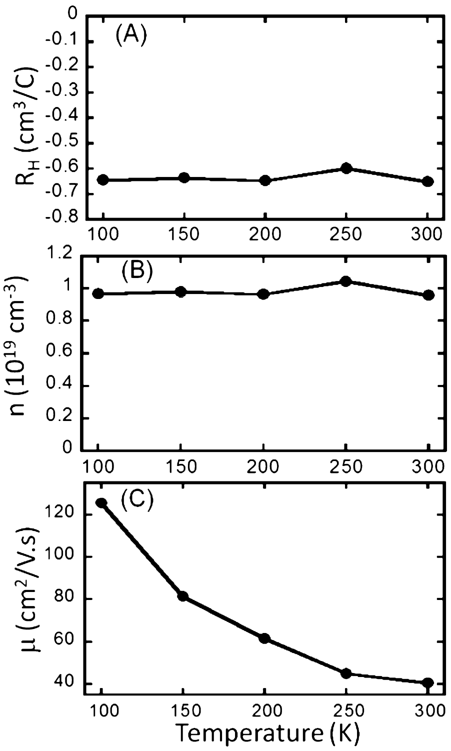

Figure 5. Low-temperature electronic transport of $Pb_7Bi_4Se_{13}$: (A) Hall coefficient; (B) carrier concentration; (C) carrier mobility.

the temperature. The temperature dependence of the thermopower with a maximum at 600 K suggests that $Pb_7Bi_4Se_{13}$ is a degenerate n-type semiconductor. Extrinsic carriers dominate electronic transport below 600 K, and the thermopower linearly increases with temperature. However, above 600 K the reduction in the thermopower suggests an onset of intrinsic carrier excitations from the valence band to the conduction band. The observed value of the thermopower at 300 K is 45% larger than the value of -110 μV K^{-1} reported for n-type PbSe doped with Pb ($n = \sim 9 \times 10^{18}$ cm^3)[51] and nearly 3 times higher than the thermopower of bulk n-type Bi_2Se_3 (-59 μV K^{-1}).[52] The band gap of $Pb_7Bi_4Se_{13}$ can be estimated using the expression E_g (eV) = $2S_{max}T_{max}$, where S_{max} (V K^{-1}) is the maximum value of the thermopower and T_{max} (K) is the temperature of the maximum thermopower.[53] The band gap of $Pb_7Bi_4Se_{13}$ calculated using the above equation is $E_g = 0.29$ eV. This value of the band gap is comparable to the reported band gap for PbSe (0.27–0.31 eV)[54] and is slightly lower than the band gap of Bi_2Se_3 ($E_g = 0.35$ eV).[30] The estimated value of the band gap of $Pb_7Bi_4Se_{13}$ is in reasonable agreement with the indirect band-gap value of 0.23 eV obtained from the electronic structure calculation (Figure 3) and is consistent with the optical band gap of ~0.29 eV extracted from diffuse-reflectance measurement (Figure 1C).

The electrical resistivity of $Pb_7Bi_4Se_{13}$ is 176 $\mu\Omega$ m at 300 K and increases with rising temperature, reaching a maximum of 282 $\mu\Omega$ m at 520 K, where the intrinsic conduction sets in. The resistivity decreases drastically with a further increase in the temperature, reaching a value of 166 $\mu\Omega$ m at 775 K (Figure 6A). The temperature dependence of the electrical resistivity is consistent with the observed temperature dependence of the thermopower and also confirms that the synthesized polycrystalline phase of $Pb_7Bi_4Se_{13}$ is a heavily doped n-type semiconductor. However, the observed value of the electrical resistivity at 300 K is 2 orders of magnitude larger than the electrical resistivity of n-type PbTe (10 $\mu\Omega$ m)[55] and Bi_2Se_3 (3.3 $\mu\Omega$ m).[52] The relatively large values of the electrical resistivity for $Pb_7Bi_4Se_{13}$ arise from low carrier mobility presumably because of (1) electron scattering at the high-density incoherent interfaces between layers A and B within the crystal structure and (2) the poor crystallinity of the sample.

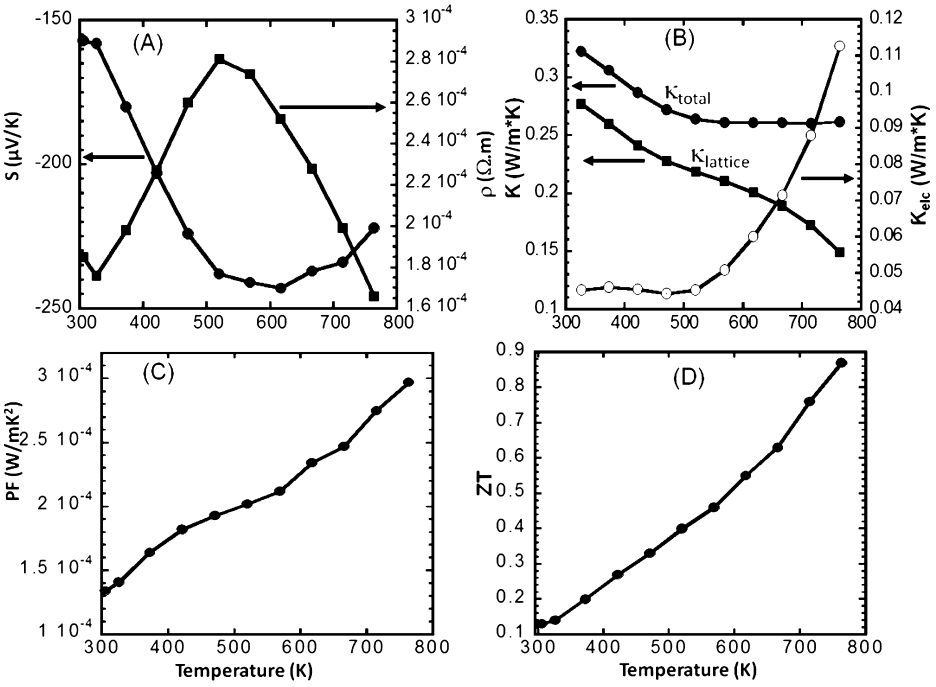

Figure 6. High-temperature thermoelectric properties of $Pb_7Bi_4Se_{13}$: (A) electrical conductivity and thermopower; (B) thermal conductivity; (C) power factor; (D) figure of merit.

Figure 6B shows the temperature dependence of the thermal conductivity of $Pb_7Bi_4Se_{13}$. At 300 K, a remarkably low total thermal conductivity of ~0.33 W m^{-1} K^{-1} was measured from a 97% dense hot-pressed pellet of $Pb_7Bi_4Se_{13}$. Interestingly, the total thermal conductivity decreases linearly with rising temperature, reaching a minimum value of 0.26 W m^{-1} K^{-1} at 520 K, and remains constant with a further increase in the temperature. The drop in the total thermal conductivity with rising temperature indicates that below 520 K the thermal conductivity is dominated by the phonon (lattice) contribution. The lattice contribution to the total thermal conductivity (κ_{lattice}) was estimated by subtracting the electronic contribution calculated using the Wiedemann−Franz law ($\kappa_{\text{el}} = L\sigma T$, where $L = 2.45 \times 10^{-8}$ W Ω K^{-2} is the Lorenz number) from the observed total thermal conductivity (Figure 6B). This results in a lattice thermal conductivity of 0.29 W m^{-1} K^{-1} at 300 K, which further decreases with rising temperature to a glasslike thermal conductivity of 0.17 W m^{-1} K^{-1} at 775 K. This extremely low value of the lattice thermal conductivity suggests that the phonon mean-free path in the $Pb_7Bi_4Se_{13}$ structure is quite small. The lattice thermal conductivity of $Pb_7Bi_4Se_{13}$ is significantly smaller than the values reported for promising thermoelectric materials such as Pb-doped PbSe (2.5 W m^{-1} K^{-1} at 300 K)[51] and Bi_2Se_3 (4 W m^{-1} K^{-1} at 300 K)[56] and is comparable to the thermal conductivity reported for $LiPbSb_3S_6$ (0.24 W m^{-1} K^{-1} at 300 K)[57] and the high-performance thermoelectric material SnSe (0.5 W m^{-1} K^{-1} at 300 K).[57] Because the sample used for the thermal conductivity measurement was obtained by a combination of mechanical alloying and thermal annealing at 773 K for 14 days, any nanoscale grains that might have been produced during mechanical alloying have likely grown into microscale-size grains during the long annealing step. Therefore, we do not expect nanometer-scale grain size to play any role in the reduction of the thermal conductivity of $Pb_7Bi_4Se_{13}$. However, the very low lattice thermal conductivity observed for $Pb_7Bi_4Se_{13}$ can be rationalized by taking into account the chemical composition and structural details. For instance, the high mean atomic weight arising from the presence of heavy elements such as Pb, Bi, and Se within the same crystal structure is expected to reduce the phonon energy, leading to a low acoustic phonon group velocity and therefore small lattice thermal conductivity.[58] In addition, these heavy elements in the crystal structure of $Pb_7Bi_4Se_{13}$ are arranged in NaCl-type layers (A and B) with various thicknesses, which are weakly stitched together by isolated chains of a face-sharing monocapped trigonal prism around Pb atoms. The alignment of atomic lattice planes in adjacent layers A and B deviates by more than 48°, which significantly reduces the propagation of the thermal phonon along the *c* axis. Therefore, the interfaces (A/B) between layers A and B in the crystal structure are highly incoherent, which is favorable for phonon scattering. Each unit cell volume of $Pb_7Bi_4Se_{13}$ contains two such interfaces, leading to a very high volume density of $\sim 1.5 \times 10^{+21}$ cm^{-3}. Phonon scattering by the high density of incoherent interfaces between layers A and B is believed to be the main contributing factor, leading to the extremely low thermal conductivity of $Pb_7Bi_4Se_{13}$. The above-mentioned structural features leading to the extremely low lattice thermal conductivity of $Pb_7Bi_4Se_{13}$ are common to all lillianite homologues with the general composition $Pb_{N-1}Bi_2Se_{N+2}$ ($N > 1$), indicating that a large number of low-thermal-conductivity and high-figure-of-merit materials can be discovered from this large family of compounds.

The temperature dependence of the power factor (PF) is shown in Figure 6C. The observed large thermopower and comparatively low electrical resistivity of $Pb_7Bi_4Se_{13}$ at 300 K resulted in a moderate PF of ~134 μW m^{-1} K^{-2}. Interestingly, the PF rapidly increases with rising temperature, reaching a value as high as 300 μW m^{-1} K^{-2} at 775 K. Although the PF is quite small compared to fully optimized high-performance thermoelectric materials such as $Bi_{2-x}Sb_xTe_3$ (~2000 μW m^{-1} K^{-2} at 250 K),[59] the extremely low total thermal conductivity leads to remarkable values of the figure of merit (Figure 6D) for $Pb_7Bi_4Se_{13}$ at temperatures suitable for energy production from waste heat. At 300 K, the *ZT* value is ~0.1 and rapidly increases with rising temperature, approaching *ZT* ~ 0.9 at 775 K. This is a very promising value for an unoptimized material. The high thermopower and inherently low thermal conductivity values of $Pb_7Bi_4Se_{13}$ point to the possibility of further enhancing the overall *ZT* by optimizing the charge carrier density via doping.

■ CONCLUSION

In summary, we have synthesized and elucidated the structure of $Pb_7Bi_4Se_{13}$ using single-crystal X-ray diffraction data. The compound corresponds to the member with $N = 4.5$ ($^{4,5}L$) of the broad family of lillianite homologous series with the general formula $Pb_{N-1}Bi_2Se_{N+2}$. Electronic structure calculations and diffuse-reflectance measurements confirmed that $Pb_7Bi_4Se_{13}$ is a narrow-gap semiconductor with a calculated indirect band gap of 0.23 eV and an optical gap of 0.29 eV. Electronic-transport measurement of the synthesized polycrystalline powder revealed n-type degenerate semiconducting behavior with large thermopower values (~−160 μV K^{-1} at 300 K) and somewhat high electrical resistivity. Interestingly, the synthesized n-type $Pb_7Bi_4Se_{13}$ exhibits extremely low thermal conductivity values ranging from 0.33 W m^{-1} K^{-1} at 300 K to 0.26 W m^{-1} K^{-1} at 775 K. The low thermal conductivity of $Pb_7Bi_4Se_{13}$ is attributed to the heavy constituent elements and to enhanced phonon scattering on the high density of atomic-scale incoherent interfaces between adjacent layers A and B in the crystal structure. The low thermal conductivity of $Pb_7Bi_4Se_{13}$ coupled with the large thermopower leads to quite promising values of the thermoelectric figure of merit, reaching as high as *ZT* ~ 0.9 at 775 K. This promising figure of merit is obtained with nonoptimized $Pb_7Bi_4Se_{13}$ that has a rather high electrical resistivity. Therefore, much higher *ZT* values can be obtained by carefully optimizing the carrier density and electrical conductivity of $Pb_7Bi_4Se_{13}$ via doping and by improving the crystallinity of the synthesized material. The observed promising thermoelectric behavior of $Pb_7Bi_4Se_{13}$, and particularly its very low intrinsic thermal conductivity, suggests that the $Pb_{N-1}Bi_2Se_{N+2}$ homologous series may be an excellent system with which to search for new high-performance thermoelectric materials. The investigation of missing members of this broad series is underway.

■ ASSOCIATED CONTENT

Ⓢ Supporting Information

CIF files for the structure refinement of $Pb_7Bi_4Se_{13}$ at different temperatures. This material is available free of charge via the Internet at http://pubs.acs.org.

AUTHOR INFORMATION

Corresponding Authors

*E-mail: kioup@umich.edu.
*E-mail: ppoudeup@umich.edu.

Author Contributions

‡A.O., G.S., and H.D. contributed to this work equally.

Notes

The authors declare no competing financial interest.

ACKNOWLEDGMENTS

This work was supported by the National Science Foundation Career Award DMR-1237550. P.F.P.P. and C.U. also gratefully acknowledge partial financial support from the U.S. Department of Energy, Office of Basic Energy Sciences, under Award DE-SC-0008574. G.S. was supported as part of the Center for Solar and Thermal Energy Conversion, an Energy Frontier Research Center funded by the Office of Science of U.S. Department of Energy, Office of Basic Energy Sciences. under Award DE- SC0000957 (computational studies). Computational resources were provided by the National Energy Research Scientific Computing Center, supported by the Office of Science of the U.S. Department of Energy under Contract DE-AC02-05CH11231.

DEDICATION

Dedicated to the memory of Professor John Corbett.

REFERENCES

(1) Biswas, K.; He, J. Q.; Blum, I. D.; Wu, C. I.; Hogan, T. P.; Seidman, D. N.; Dravid, V. P.; Kanatzidis, M. G. *Nature* **2012**, *489*, 414−418.

(2) Poudeu, P. F. P.; D'Angelo, J.; Downey, A. D.; Short, J. L.; Hogan, T. P.; Kanatzidis, M. G. *Angew. Chem., Int. Ed.* **2006**, *45*, 3835−3839.

(3) Zhao, L. D.; Lo, S. H.; Zhang, Y. S.; Sun, H.; Tan, G. J.; Uher, C.; Wolverton, C.; Dravid, V. P.; Kanatzidis, M. G. *Nature* **2014**, *508*, 373−377.

(4) Liu, H. L.; Shi, X.; Xu, F. F.; Zhang, L. L.; Zhang, W. Q.; Chen, L. D.; Li, Q.; Uher, C.; Day, T.; Snyder, G. J. *Nat. Mater.* **2012**, *11*, 422−425.

(5) Jackson, P.; Hariskos, D.; Lotter, E.; Paetel, S.; Wuerz, R.; Menner, R.; Wischmann, W.; Powalla, M. *Prog. Photovoltaics* **2011**, *19*, 894−897.

(6) Riha, S. C.; Johnson, D. C.; Prieto, A. L. *J. Am. Chem. Soc.* **2011**, *133*, 1383−1390.

(7) Djieutedjeu, H.; Poudeu, P. F. P.; Takas, N. J.; Makongo, J. P. A.; Rotaru, A.; Ranmohotti, K. G. S.; Anglin, C. J.; Spinu, L.; Wiley, J. B. *Angew. Chem., Int. Ed.* **2010**, *49*, 9977−9981.

(8) Ranmohotti, K. G. S.; Djieutedjeu, H.; Poudeu, P. F. P. *J. Am. Chem. Soc.* **2012**, *134*, 14033−14042.

(9) Poudeu, P. F. P.; Djieutedjeu, H.; Ranmohotti, K. G. S.; Makongo, J. P. A. M.; Takas, N. *Inorg. Chem.* **2014**, *53*, 209−220.

(10) Kanatzidis, M. G. *Acc. Chem. Res.* **2005**, *38*, 359−368.

(11) Mrotzek, A.; Kanatzidis, M. G. *Acc. Chem. Res.* **2003**, *36*, 111−119.

(12) Ruck, M.; Poudeu, P. F. P. *Z. Anorg. Allg. Chem.* **2008**, *634*, 475−481.

(13) Ruck, M.; Poudeu, P. F. P. *Z. Anorg. Allg. Chem.* **2008**, *634*, 482−490.

(14) Makovicky, B.; Mumme, W. C.; Watts, J. A. *Can. Mineral.* **1977**, *15*, 339−348.

(15) Pring, A.; Jercher, M.; Makovicky, E. *Mineral. Mag.* **1999**, *63*, 917−926.

(16) Topa, D.; Makovicky, E.; Schimper, H. J.; Dittrich, H. *Can. Mineral.* **2010**, *48*, 1127−1135.

(17) Takagi, J.; Takeuchi, Y. *Acta Crystallogr.* **1972**, *B28*, 649−651.

(18) Takeuchi, Y.; Takagi, J. *Proc. Jpn. Acad.* **1974**, *50*, 76−79.

(19) Iitaka, Y.; Nowacki, W. *Acta Crystallogr.* **1962**, *15*, 691−698.

(20) Chung, D.-Y.; Lane, M. A.; Ireland, J. R.; Brazis, P. W.; Kannewurf, C. R.; Kanatzidis, M. G. *Mater. Res. Soc. Symp.* **2000**, *626*, Z7.4.1.

(21) Agaev, K. A.; Talybov, A. G.; Semileto, Sa. *Kristallografiya* **1966**, *11*, 736−740.

(22) Agaev, K. A.; Semileto, Sa. *Sov. Phys. Crystallogr.* **1968**, *13*, 201−203.

(23) Liu, H. F.; Chang, L. L. Y. *Am. Mineral.* **1994**, *79*, 1159−1166.

(24) Zhang, Y. G.; Wilkinson, A. P.; Lee, P. L.; Shastri, S. D.; Shu, D. M.; Chung, D. Y.; Kanatzidis, M. G. *J. Appl. Crystallogr.* **2005**, *38*, 433−441.

(25) Zemskov, V. S.; Shelimova, L. E.; Konstantinov, P. P.; Avilov, E. S.; Kretova, M. A.; Nikhezina, I. Y. *Inorg. Mater.: Appl. Res.* **2011**, *2*, 405−413.

(26) Riley, D. J.; Waggett, J. P.; Wijayantha, K. G. U. *J. Mater. Chem.* **2004**, *14*, 704−708.

(27) Kang, I.; Wise, F. W. *J. Opt. Soc. Am. B* **1997**, *14*, 1632−1646.

(28) Abd-Elkader, O. H.; Deraz, N. M. *Int. J. Mol. Sci.* **2014**, *15*, 1842−1851.

(29) Wang, H.; Pei, Y. Z.; LaLonde, A. D.; Snyder, G. J. *Proc. Natl. Acad. Sci. U.S.A.* **2012**, *109*, 9705−9709.

(30) Hor, Y. S.; Richardella, A.; Roushan, P.; Xia, Y.; Checkelsky, J. G.; Yazdani, A.; Hasan, M. Z.; Ong, N. P.; Cava, R. J. *Phys. Rev. B* **2009**, *79*, 195208.

(31) Kotuem, G. *Reflectance Spectroscopy*; Ed. New York, 1969.

(32) Wendlandt, W. W.; Hecht, H. G. *Reflectance Spectroscopy*; Intersceince Publishers: New York, 1966.

(33) Sheldrick, G. M. *SHELTXL*; Bruker Analytical X-ray Instruments Inc.: Madison, WI, 2000.

(34) Brese, N. E.; Okeeffe, M. *Acta Crystallogr., Sect. B* **1991**, *47*, 192−197.

(35) Brandenburg, K. *Diamond*; Crystal Impact GbR: Bonn, Germany, 2005.

(36) Perdew, J. P.; Zunger, A. *Phys. Rev. B* **1981**, *23*, 5048−5079.

(37) Ihm, J.; Zunger, A.; Cohen, M. L. *J. Phys. C Solid State* **1979**, *12*, 4409−4422.

(38) Troullier, N.; Martins, J. L. *Phys. Rev. B* **1991**, *43*, 1993−2006.

(39) Giannozzi, P.; Baroni, S.; Bonini, N.; Calandra, M.; Car, R.; Cavazzoni, C.; Ceresoli, D.; Chiarotti, G. L.; Cococcioni, M.; Dabo, I.; Dal Corso, A.; de Gironcoli, S.; Fabris, S.; Fratesi, G.; Gebauer, R.; Gerstmann, U.; Gougoussis, C.; Kokalj, A.; Lazzeri, M.; Martin-Samos, L.; Marzari, N.; Mauri, F.; Mazzarello, R.; Paolini, S.; Pasquarello, A.; Paulatto, L.; Sbraccia, C.; Scandolo, S.; Sclauzero, G.; Seitsonen, A. P.; Smogunov, A.; Umari, P.; Wentzcovitch, R. M. *J. Phys.: Condens. Matter* **2009**, *21*, 395502.

(40) Yazyev, O. V.; Kioupakis, E.; Moore, J. E.; Louie, S. G. *Phys. Rev. B* **2012**, *85*, 161101.

(41) Kioupakis, E.; Tiago, M. L.; Louie, S. G. *Phys. Rev. B* **2010**, *82*, 245203.

(42) Monkhorst, H. J.; Pack, J. D. *Phys. Rev. B* **1976**, *13*, 5188−5192.

(43) Hybertsen, M. S.; Louie, S. G. *Phys. Rev. B* **1986**, *34*, 5390−5413.

(44) Deslippe, J.; Samsonidze, G.; Strubbe, D. A.; Jain, M.; Cohen, M. L.; Louie, S. G. *Comput. Phys. Commun.* **2012**, *183*, 1269−1289.

(45) Hybertsen, M. S.; Louie, S. G. *Phys. Rev. B* **1986**, *34*, 2920−2922.

(46) Deslippe, J.; Samsonidze, G.; Jain, M.; Cohen, M. L.; Louie, S. G. *Phys. Rev. B* **2013**, *87*, 165124.

(47) Mrotzek, A.; Kanatzidis, M. G. *Inorg. Chem.* **2003**, *42*, 7200−7206.

(48) Setyawan, W.; Curtarolo, S. *Comput. Mater. Sci.* **2010**, *49*, 299−312.

(49) Szymanski, J. E. *Basic Mathematics for Electronic Engineers: Models and Applications*; Taylor & Francis: London, 1989.

(50) Sze, S. M. *Physics of Semiconductor Devices*, 2nd ed.; Wiley: New York, 1981.

(51) Androulakis, J.; Chung, D. Y.; Su, X. L.; Zhang, L.; Uher, C.; Hasapis, T. C.; Hatzikraniotis, E.; Paraskevopoulos, K. M.; Kanatzidis, M. G. *Phys. Rev. B* **2011**, *84*, 155207.

(52) Navratil, J.; Horak, J.; Plechacek, T.; Kamba, S.; Lost'ak, P.; Dyck, J. S.; Chen, W.; Uher, C. *J. Solid State Chem.* **2004**, *177*, 1704−1712.

(53) Goldsmid, H. J.; Sharp, J. W. *J. Electron. Mater.* **1999**, *28*, 869−872.

(54) Scanlon, W. W. *Solid State Phys.* **1959**, *9*, 83−137.

(55) Androulakis, J.; Lee, Y.; Todorov, I.; Chung, D. Y.; Kanatzidis, M. *Phys. Rev. B* **2011**, *83*, 195209.

(56) Janicek, P.; Drasar, C.; Benes, L.; Lost'ak, P. *Cryst. Res. Technol.* **2009**, *44*, 505−510.

(57) Agha, E. C.; Malliakas, C. D.; Im, J.; Jin, H. S.; Zhao, L. D.; Freeman, A. J.; Kanatzidis, M. G. *Inorg. Chem.* **2014**, *53*, 673−675.

(58) Rowe, D. M. *Thermoelectrics and its energy harvesting*; CRC Press: Boca Raton, FL, 2012.

(59) Poudel, B.; Hao, Q.; Ma, Y.; Lan, Y. C.; Minnich, A.; Yu, B.; Yan, X. A.; Wang, D. Z.; Muto, A.; Vashaee, D.; Chen, X. Y.; Liu, J. M.; Dresselhaus, M. S.; Chen, G.; Ren, Z. F. *Science* **2008**, *320*, 634−638.